Sensors and Materials, Vol. 35, No. 7 (2023) 2483–2499
MYU Tokyo

S & M 3336

Effect of Laser Intensity on an Electron's Optimal Position and Spatial Radiation Characteristics in a Linearly Polarized Tightly Focused Laser Field

Hanchen Qiu,[1] Youwei Tian,[2*] and Chih-Cheng Chen[3,4**]

[1]School of Computer Science, Nanjing University of Posts and Telecommunications, Nanjing 210023, China
[2]College of Science, Nanjing University of Posts and Telecommunications, Nanjing 210023, China
[3]Department of Automatic Control Engineering, Feng Chia University, Taichung 40724, Taiwan
[4]Department of Aeronautical Engineering, Chaoyang University of Technology, Taichung 413, Taiwan

(Received April 15, 2023; accepted June 5, 2023)

Keywords: optical imaging, nonlinear Thomson scattering, laser intensity, optimal position, spatial radiation, numerical simulation

X-rays are widely used in the field of optical imaging. A novel type of X-ray source is the relativistic nonlinear Thomson scattering (RNTS). Within the framework of RNTS, we investigated in detail the effects of different intensities of linearly polarized tightly focused lasers on the maximum radiation power, optimal position of an electron (initial position of the electron that yields the maximum radiation power in the entire space), as well as the motion and spatial radiation features of the electron at the optimal position. Our results reveal, for the first time, that the optimal position and maximum radiation power of the electron exhibit significant linear and exponential dependences, respectively, on the laser amplitude. After interacting with the laser, the initially stationary electron at the optimal position first undergoes an oscillatory motion and then moves linearly. The entire trajectory of the electron is asymmetric. As the laser intensity increases, the spatial and angular distributions of the radiation become smaller, and the collimation of radiation increases. In the direction of maximum power radiation, the azimuth angle φ remains at 0°, whereas the corresponding polar angle θ decreases from 41° to 20°, indicating that the spatial radiation approaches the z-axis. The time when the maximum radiation power is obtained is approximately 50.7 fs. Additionally, the asymmetry and micro-double-peak structure of the temporal spectra, as well as the modulation characteristics of the frequency spectra, were further investigated in the direction of the maximum power radiation. These findings will assist researchers in achieving high-power and ultrashort X-rays in experiments, thereby increasing the resolution and imaging speed of optical imaging.

1. Introduction

X-rays are extensively utilized in various optical imaging fields, such as computed tomography[1,2] and biomedical imaging.[3,4] To improve the resolution and speed of optical imaging, researchers have been exploring novel X-ray sources. Since the late 1980s, the field of

*Corresponding author: e-mail: tianyw@njupt.edu.cn
**Corresponding author: e-mail: chenccheng@fcu.edu.tw
https://doi.org/10.18494/SAM4455

ISSN 0914-4935

high-power lasers and matter interaction has flourished[5,6] owing to the emergence of Chirped Pulse Amplification (CPA) technology.[7–9] Consequently, research on relativistic nonlinear Thomson scattering (RNTS) as a promising X-ray source has attracted increasing attention.[10,11]

Thomson scattering occurs when a free charged particle is subjected to an electromagnetic field, and the Doppler frequency shift often makes this process nonlinear. Extensive research has been conducted to investigate the spatial radiation characteristics of nonlinear Thomson scattering in order to better obtain high-quality X-rays. Back in 2003, Lee *et al.* studied the RNTS of an initially stationary single electron in a strong laser field.[12] They analyzed the spatial characteristics of the radiation and the interesting modulation structure of the energy spectrum. By varying the incident laser intensity, Li *et al.* found that the spatial radiation exhibits a bifoliate shape when a linearly polarized laser is used.[13] The electron trajectory and the spatial radiation spectrum resulting from the interaction between the circularly polarized laser of different intensities and the stationary electron are discussed in Wang *et al.*'s paper.[14] Hong *et al.* observed that increasing the laser intensity of a tightly focused Gaussian laser can break the symmetry of electron trajectories and enhance the peak.[15] The effect of laser intensity on the emission spectrum was studied by Zhuang *et al.*, who found that the spectral bandwidth of the emitted light becomes larger in a high-intensity laser field.[16] In addition, Yan *et al.* studied the effect of the initial position of the high-energy electron on its spatial radiation properties.[17] It was discovered that the maximum spatial radiation energy is attained when the electron's initial position is $(0, 0, -7\lambda_0)$. To date, no pertinent research has been found that establishes a connection between the laser intensity and the optimal position of an electron. While Yan *et al.* identified the optimal position of the electron, they were restricted to studying the spatial radiation characteristics of a particular laser intensity (amplitude $a_0 = 6$).[17] However, our experimental results show that the changing laser intensity significantly affects the optimal position of the electron and the corresponding maximum radiation power (as shown in Sect. 3.1). Although Borovskiy and Galkin proposed that the optimal position exhibits symmetric trajectories and found that electron energy saturates with increasing laser intensity based on the dipole approximation,[18] our study revealed that the electron trajectories at the optimal position do not possess symmetry as illustrated in Sect. 3.2. Moreover, we observed that the electron energy increases exponentially with the laser intensity [as depicted in Fig. 2(b)], instead of tending toward saturation. We provide a detailed discussion of these findings and explore potential reasons for the observed discrepancies. In practical applications, researchers are primarily concerned with where they can obtain the maximum radiation power and generate ultrashort X-rays. Therefore, investigating the variation of the optimal position with respect to laser intensity is crucial for comprehending and utilizing RNTS radiation. In this study, we investigate the impact of varying laser intensities on the optimal electron position in relativistic nonlinear Thomson scattering through theoretical analyses and numerical simulations. Our results demonstrate that there is a significant linear relationship between the electron's optimal position z_0 and the laser amplitude a_0, which can be described by the mathematical equation $z_0 = -2 \times a_0 + 3$. Additionally, we have carried out an analysis of the impact of the azimuth angle φ and the polar angle θ on electron radiation power in order to determine the direction that yields the maximum radiation power for varying laser intensities.

The remaining sections of this paper are as follows: In Sect. 2, we construct an RNTS model of the interaction between the electron and laser pulse, and the analytical expressions of the laser pulse vector potential, electron motion law, and RNTS are derived. In Sect. 3, the maximum radiation power and the electron's corresponding optimal position for different laser intensities are obtained. The effects of the laser intensity on the dynamics, spatial radiation distribution, radiation time spectra, and frequency spectra of the electron in the best position are analyzed. In Sect. 4, we present the main experimental conclusions, propose the application prospects of the findings, and discuss the remaining limitations and possible solutions for future work.

2. Model and Theoretical Formulas

2.1 Gaussian laser pulse and electron motion

In tightly focused lasers, the paraxial approximation loses validity, and higher order field effects become necessary. We model the laser beam with a vector potential linearly polarized along the +x axis, which allows us to derive the following components of the electric field.[19,20]

$$E_x = E\left\{S_0 + \varepsilon^2\left[\xi^2 S_2 - \frac{\rho^4 S_3}{4}\right] + \varepsilon^4\left[\frac{S_2}{8} - \frac{\rho^2 S_3}{4} - \frac{\rho^2\left(\rho^2 - 16\xi^2\right)S_4}{16} - \frac{\rho^4\left(\rho^2 + 2\xi^2\right)S_5}{8} + \frac{\rho^8 S_6}{32}\right]\right\} \quad (1)$$

$$E_y = E\xi v\left\{\varepsilon^2 S_2 + \varepsilon^4\left[\rho^2 S_4 - \frac{\rho^4 S_5}{4}\right]\right\} \quad (2)$$

$$E_z = E\xi\left\{\varepsilon C_1 + \varepsilon^3\left[-\frac{C_2}{2} + \rho^2 C_3 - \frac{\rho^4 C_4}{4}\right] + \varepsilon^5\left[-\frac{3C_3}{8} - \frac{3\rho^2 C_4}{8} + \frac{17\rho^4 C_5}{16} - \frac{3\rho^6 C_5}{16} - \frac{3\rho^6 C_6}{8} + \frac{\rho^8 C_7}{32}\right]\right\} \quad (3)$$

Similarly, the magnetic field components can be described as

$$B_x = 0, \quad (4)$$

$$B_y = E\left\{S_0 + \varepsilon^2\left[\frac{\rho^2 S_2}{2} - \frac{\rho^4 S_3}{4}\right] + \varepsilon^4\left[-\frac{S_2}{8} + \frac{\rho^2 S_3}{4} + \frac{5\rho^4 S_4}{16} - \frac{\rho^6 S_5}{4} + \frac{\rho^8 S_6}{32}\right]\right\}, \quad (5)$$

$$B_z = Ev\left\{\varepsilon C_1 + \varepsilon^3\left[\frac{C_2}{2} + \frac{\rho^2 C_3}{2} - \frac{\rho^4 C_4}{4}\right] + \varepsilon^5\left[\frac{3C_3}{8} + \frac{3\rho^2 C_4}{8} + \frac{3\rho^4 C_5}{16} - \frac{\rho^6 C_6}{4} + \frac{\rho^8 C_7}{32}\right]\right\}. \quad (6)$$

Note that the cross section of the beam at the focus is circular with a radius of w_0, and the cross section at any point z along the axis is also circular, with a radius given by $w(z) = w_0\sqrt{1 + (z / z_r)^2}$. For $k = 2\pi/\lambda$, the Rayleigh range is $z_r = kw_0^2 / 2$. The electromagnetic

field is fifth-order expanded accurate to the diffraction angle $\varepsilon = w_0 / z_r$. For simplicity of expression, in Eqs. (1)–(6), $\xi = x / w_0, v = y / w_0$ and

$$E = E_0 \frac{w_0}{w} \exp\left[-\frac{\eta^2}{L^2} - \frac{r^2}{w^2} \right]; E = kA_0. \tag{7}$$

In Eq. (7), the pulse width L relates to the time length of the beam: $L = \tau c$, where τ is the duration of the laser. The normalized laser amplitude a_0 is related to the laser intensity I_0 as

$$a_0 = \frac{eA_0}{mc^2} = 8.5 \times 10^{-10} \lambda_0 \sqrt{I_0}. \tag{8}$$

A_0 represents the polarization amplitude, λ_0 is the laser wavelength in μm, and I_0 is the laser intensity in W/cm^2. For a laser with a wavelength of $\lambda_0 = 1$, the laser amplitude $a_0 = 1$ corresponds to a laser intensity of $I_0 = 1.38 \times 10^{18}$ W/cm^2. Among them, S_n and C_n are shown as

$$S_n = \left(\frac{w_0}{w} \right)^n \sin\left(\psi + n\psi_G \right); n = 0, 1, 2, \ldots, \tag{9}$$

$$C_n = \left(\frac{w_0}{w} \right)^n \cos\left(\psi + n\psi_G \right). \tag{10}$$

Furthermore, wave number $k = \omega/c$ and perpendicular distance $r = \sqrt{x^2 + y^2}$, $\rho = r / w_0$. By starting from a vector potential with an amplitude of A_0 and a frequency of ω, these equations can be obtained. The remaining symbols in Eqs. (9) and (10) are defined as

$$\psi = \psi_0 + \psi_p - \psi_R + \psi_G, \tag{11}$$

$$\psi_p = \eta = \omega t - kz, \tag{12}$$

$$\psi_G = \tan^{-1}\left(\frac{z}{z_r} \right), \tag{13}$$

$$\psi_R = \frac{kr^2}{2R}, \tag{14}$$

$$R\left(z \right) = z + \frac{z_r^2}{z}. \tag{15}$$

The symbol ψ_0 is the constant initial phase, the plane wave phase is ψ_p, the Guoy phase ψ_G is the total phase change of the Gaussian beam at z from $-\infty$ to $+\infty$ when the phase change is π, and ψ_R is the phase related to the wavefront curvature, where $R(z)$ is the radius of curvature of the wavefront intersecting the beam axis at the coordinate z. The fields given above satisfy Maxwell's equations $\nabla \cdot E = 0 = \nabla \cdot B$, with an additional ε^6 order term.

Using single-electron theory, we numerically solve the Lorentz equation and energy equation to determine the motion of an electron with mass m and charge $-e$ in the laser pulse.

$$\frac{\mathrm{d}\boldsymbol{p}}{\mathrm{d}t} = -e\left[\boldsymbol{E} + \boldsymbol{u} \times \boldsymbol{B}\right] \tag{16}$$

$$\frac{\mathrm{d}\kappa}{\mathrm{d}t} = -ec\boldsymbol{u} \cdot \boldsymbol{E} \tag{17}$$

In Eqs. (16) and (17), the physical quantities have their usual definitions: the momentum $\boldsymbol{p} = \gamma mc\boldsymbol{u}$, the energy $\kappa = \gamma mc^2$, the Lorentz factor $\gamma = (1 - \boldsymbol{u}^2)^{-1/2}$, and the electron velocity $\boldsymbol{u}$ is normalized to the speed of light c in vacuum. The peak field intensity I_0 will be expressed as $q = eE_0/mc\omega$, where $I_0\lambda^2 \approx 1.375 \times 10^{18} q^2$ (W/cm^2)(μm)^2. We use the Runge–Kutta–Fehlberg (RKF45) method to numerically solve the ordinary differential equations (ODEs) given by Eqs. (16) and (17) and track the position and velocity of the electron at each time step.

2.2 Angular radiation

Figure 1 illustrates the geometric schematic of the interaction between a stationary high-energy single electron and a linearly polarized tightly focused Gaussian laser pulse propagating along the z-axis direction. In the polar coordinate system, the radiation direction vector is

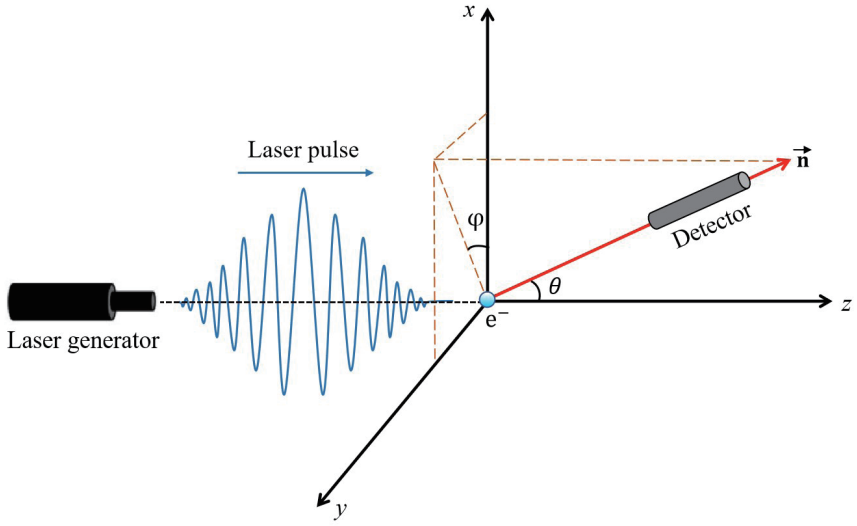

Fig. 1. (Color online) Geometric schematic of the interaction between a laser pulse propagating along the z-axis and an initially stationary electron.

defined as $\boldsymbol{n}$ = (sinθcosφ, sinθsinφ, cosθ), where θ is the polar angle and φ is the azimuth angle. At time t, the radiation power per unit solid angle can be expressed as

$$\frac{dP(t)}{d\Omega}=\left[\frac{\left|\boldsymbol{n}\times\left[\left(\boldsymbol{n}-\boldsymbol{u}\right)\times d_t\boldsymbol{u}\right]\right|^2}{(1-\boldsymbol{n}\cdot\boldsymbol{u})^6}\right]_{t'}, \tag{18}$$

where $dP(t)/d\Omega$ is normalized by $e^2\omega_0/4\pi c$, t' is the time when the electron interacts with the laser pulse, and t is the observation time, which is the delayed time relative to t'. The relationship between t and t' is given by $t = t' + R_0 - \boldsymbol{n}\cdot\boldsymbol{r}$, where R_0 refers to the distance from the interacting area to the viewing point, and $\boldsymbol{r}$ is the position vector. We assume that the viewing point is sufficiently far away from the interaction region.

During the interaction of an electron with a laser pulse, the radiation energy per unit frequency interval per unit solid angle can be expressed as

$$\frac{d^2I}{d\omega d\Omega}=\left|\int_{-\infty}^{\infty}\frac{\boldsymbol{n}\times\left[\left(\boldsymbol{n}-\boldsymbol{u}\right)\times d_t\boldsymbol{u}\right]}{(1-\boldsymbol{n}\cdot\boldsymbol{u})^2}e^{is\left(t-\boldsymbol{n}\cdot\boldsymbol{r}\right)}dt\right|^2, \tag{19}$$

where $d^2I/d\omega d\Omega$ is normalized by $e^2\omega_0/4\pi c$ and harmonic order $s = \omega_s/\omega_0$, where ω_s is the angular frequency of the scattering radiation. The spatial, temporal, and spectral characteristics of RNTS can be calculated using Eqs. (18) and (19).

3. Results and Discussion

In this section, the interaction between a linearly polarized Gaussian laser pulse and a high-energy electron is simulated. The laser pulse used is a linearly polarized laser pulse that propagates in the positive direction of the z-axis and the polarization direction is along the x-axis. The normalized laser amplitude a_0 interval of the laser is selected as [3, 10] (the corresponding laser intensity I_0 interval is [1.24 × 10^{19} Wcm^{-2}, 1.38 × 10^{20} Wcm^{-2}]), the waist radius of the beam $b_0 = 3\lambda_0$ (3 μm), the wavelength λ_0 = 1 μm, and the pulse width $L = 3\lambda_0$(10 *fs*). The initial energy of the electron is normalized to γ_0 = 1 eV (the initial velocity is 0). The electron's initial position is confined to the interval of [−25λ_0, 10λ_0] along the z-axis. For a more direct comparison of different cases, the electron radiation in Sect. 3 is normalized by its own maximum value. Note that all numerical results in this section are based on the physical laws described in Sect. 2. The term "electron's optimal position" is used to refer to the electron's initial position, which corresponds to the maximum radiation power in the entire space. Meanwhile, the laser intensity I_0 is adjusted by tuning the laser amplitude a_0.

3.1 Electron's optimal position and maximum radiation power

The variation trends of the electron's optimal position and the maximum radiation power with respect to laser intensity are investigated. As an example, we study the interaction between

an electron and a linearly polarized tightly focused laser with an amplitude of $a_0 = 6$. In particular, as shown in Fig. 2(a), the relationship between the initial electron position z and the electron radiation power $dP/d\Omega$ is examined in the range of $[-20\lambda_0, 10\lambda_0]$ with an interval of λ_0. In Fig. 2(a), the radiation power $dP/d\Omega$ increases and then decreases as the electron's initial position advances along the positive z-axis. The maximum value of 3.53×10^6 is reached at $z = -9\lambda_0$. Therefore, for a linearly polarized tightly focused laser with amplitude $a_0 = 6$, the maximum radiation power of the electron $(dP/d\Omega)_{max}$ and the optimal position z_0 are 3.53×10^6 and $-9\lambda_0$, respectively. Note that in the range $[-20\lambda_0, \lambda_0]$, the radiation power $dP/d\Omega$ exhibits a certain symmetry around $z = -9\lambda_0$. To further investigate the effect of laser intensity on the electron, the maximum radiation power $(dP/d\Omega)_{max}$ and the corresponding optimal position of the electron z_0 are calculated for different laser amplitudes a_0, as shown in Fig. 2(b).

In Fig. 2(b), the measured maximum electron radiation power $(dP/d\Omega)_{max}$ and the electron's optimal position z_0 are fitted exponentially and linearly, respectively. The fitting results are

$$\left(\frac{dP}{d\Omega}\right)_{max} = 25850 \times e^{0.93 a_0}, \tag{20}$$

$$z_0 = -2 \times a_0 + 3. \tag{21}$$

The goodness of fit in Eqs. (20) and (21) is extremely high, with the R-squares of 0.999 and 1.000, respectively (precision of 1×10^{-3}), indicating a good fitting effect. The study illustrates that as the laser intensity increases, the electron's maximum radiation power $(dP/d\Omega)_{max}$ increases exponentially with respect to a_0, whereas the optimal position z_0 shifts linearly to the left with respect to a_0. In contrast to Borovskiy and Galkin's work,[18] which adopts a dipole approximation and shows saturation of the electron radiation, our results show that the electron

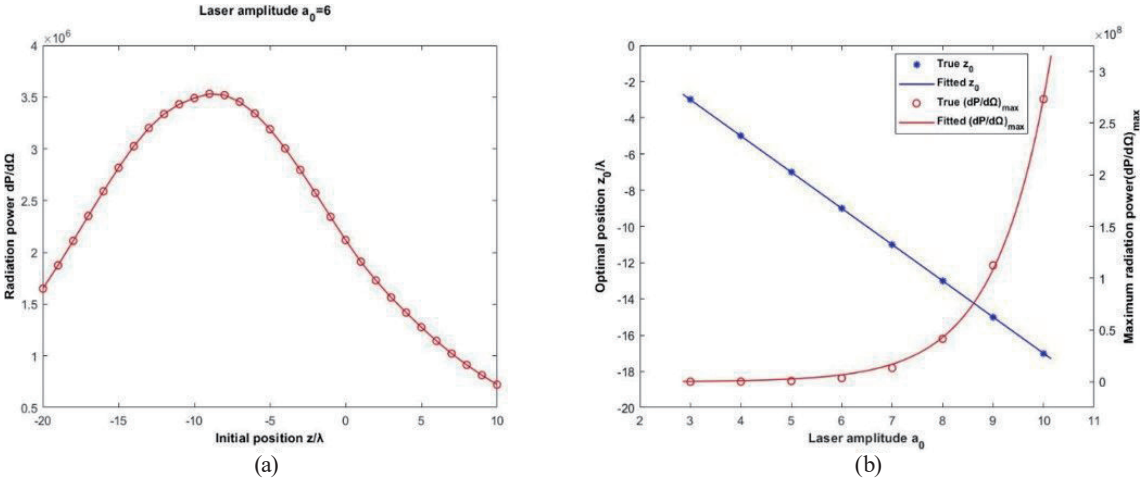

Fig. 2. (Color online) (a) Variation trend of the electron radiation power $dp/d\Omega$ with respect to the initial electron position z when $a_0 = 6$. (b) Scatter plot and fitting curve of the maximum radiation power $(dp/d\Omega)_{max}$ (circular markers, red line) and the optimal position z_0 (asterisk markers, blue line) of the electron corresponding to different laser amplitudes ($a_0 = 3, 4, 5, \ldots, 10$).

radiation increases exponentially with increasing laser intensity, as depicted by the red line in Fig. 2(b).

3.2 Electron trajectories

Figure 3 illustrates the trajectories of the electron initially located at its respective optimal position z_0, under linearly polarized laser pulses of different intensities. By substituting the polarization vector of the laser pulse into Eqs. (16) and (17), we can derive the electron trajectory throughout the process of the interaction. As expected, the greater the laser intensity I_0, the larger the amplitude of the electron motion.

Figure 3 shows that the electrons at the optimal position under different laser intensities have basically the same motion pattern. The electrons first oscillate in the *xoz* plane and then move linearly along the positive direction of the *z*-axis. The oscillating motion of the electron can be divided into two phases: acceleration and deceleration. The amplitude increases during the acceleration phase, which starts from the beginning to the middle of the pulse, and then decreases during the deceleration phase, which extends from the middle to the end of the pulse. Owing to the presence of the negative exponential term $\exp(-\eta^2/L^2-r^2/w^2)$ in the vector Eq. (7), the change in the vectorial potential decreases as the electron moves. Consequently, the deceleration process tends to be more time-consuming than the acceleration process. In addition, the combination of the time-invariant oscillation period of the electron and the time-varying transverse and longitudinal velocities leads to an increase followed by a decrease in the amplitude of oscillation and the distance traveled transversely during a single period of oscillation. Furthermore, as the laser intensity increases, the duration of the electron–laser interaction as well as the maximum oscillation amplitude and the transverse displacement of the electron gradually increase.

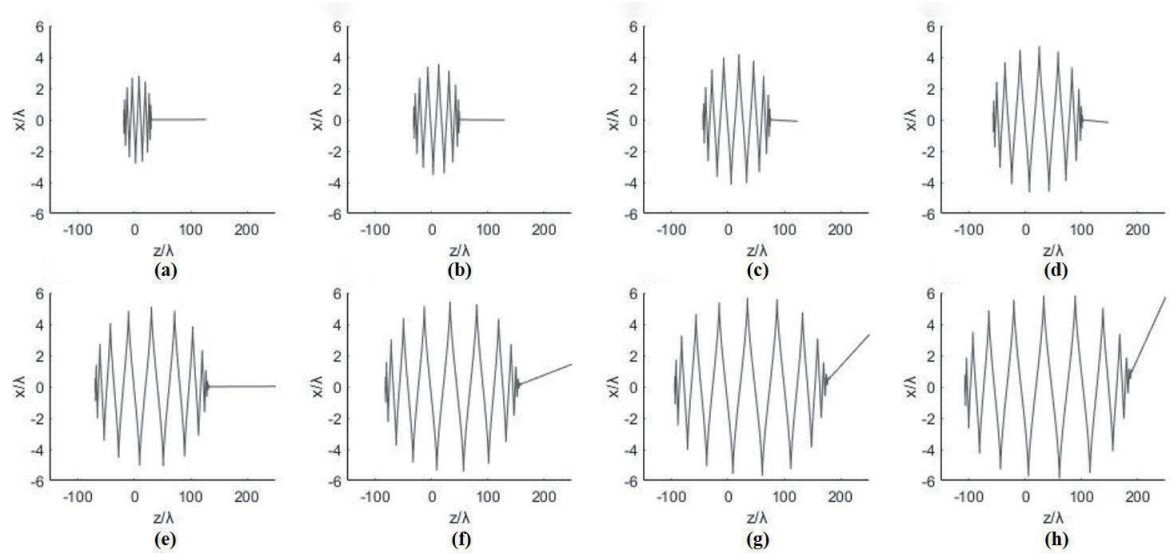

Fig. 3. Motion trajectory diagrams of electrons located at the optimal position corresponding to lasers with different intensities. Subplots (a)–(h) correspond to a_0 = 3, 4, 5, …, 10, respectively.

As shown in Fig. 3, we found that the electron trajectories are not symmetric about $z = 0$, which is different from the symmetric trajectories with the maximum electron radiation revealed in Borovskiy and Galkin's work.[18] This is because the laser intensity experienced by the electron at different positions is not symmetric about $z = 0$ during the interaction with the tightly focused laser pulse, leading to the asymmetry of the electron motion trajectory. Moreover, it should be emphasized that the electron trajectories reported in Borovskiy and Galkin's study show an asymmetry with respect to the $z = 0$.[18]

3.3 Spatial distribution of radiation

In this section, the spatial distribution of radiation has been studied in different coordinate systems, including Cartesian, spherical, and polar coordinates. In the Cartesian coordinate system, the angular distribution of electron radiation power in the whole space is calculated. As shown in Fig. 4, the radiation takes on the shape of two leaves and is asymmetric about the *yoz* plane. As the laser intensity increases, this asymmetry becomes more pronounced. The two "leaves" gradually become thinner and closer to the *z*-axis, while the angle between their radiation direction and the *z*-axis gradually decreases. This is because as the intensity of the laser increases, the acceleration and velocity of the electron increase, leading to a smaller radiation space and a gradual thinning of the radiation branches. Meanwhile, the longitudinal ponderomotive force increases, causing the electron to move closer to the *z*-axis, and thus the two branches gradually move closer to the *z*-axis.

In the spherical coordinate system, the spatial radiation power generated by the electron in Fig. 5 was projected into the transverse plane perpendicular to the *z*-axis direction and

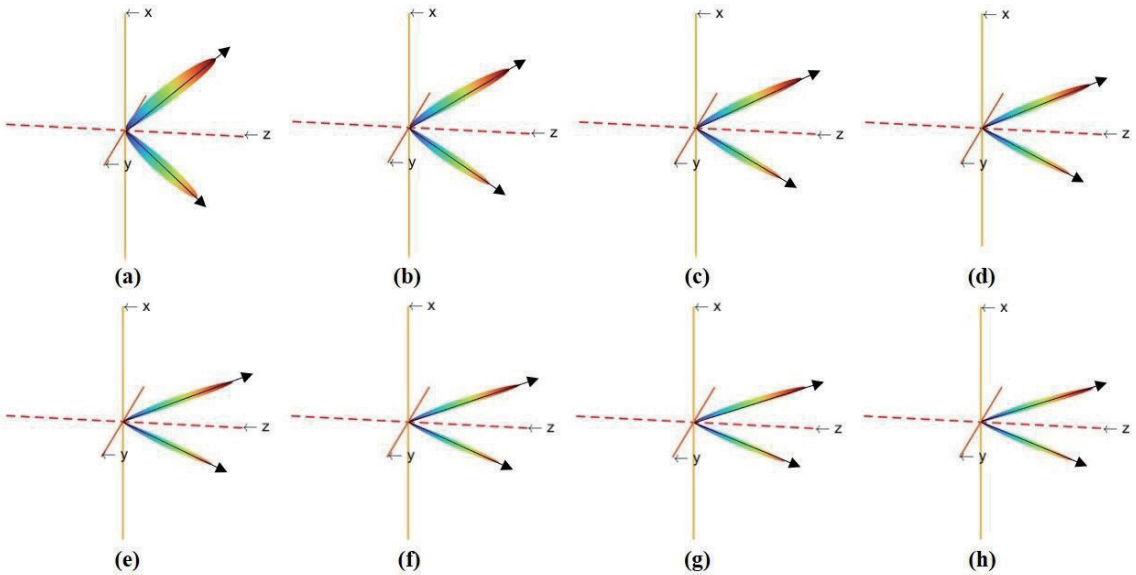

Fig. 4. (Color online) Angular distribution of electron radiation power under different laser intensities. Subplots (a)–(h) correspond to $a_0 = 3, 4, 5, \ldots, 10$, respectively. The black arrow shows the direction of radiation, and the radiation power is normalized by its own maximum value.

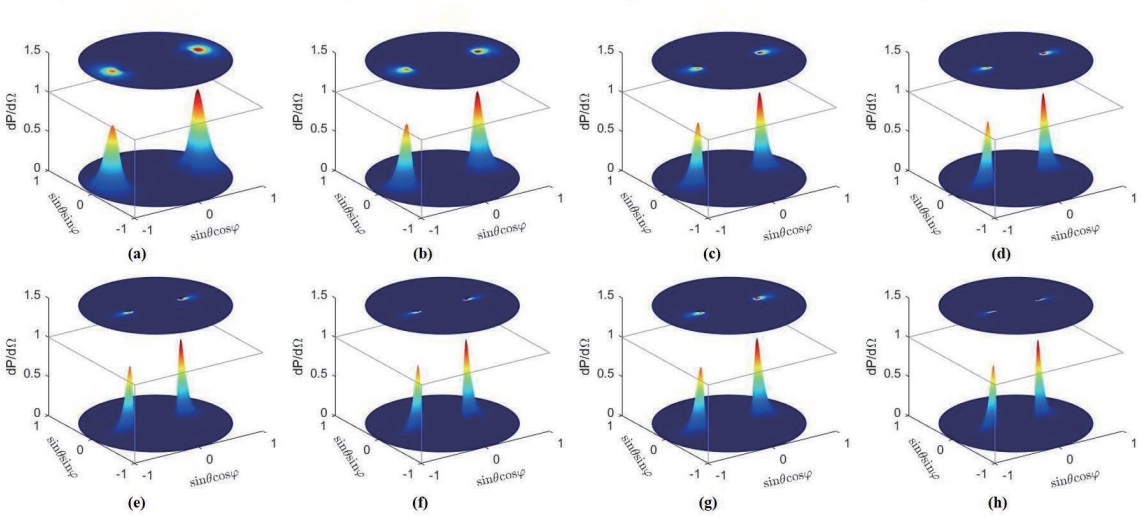

Fig. 5. (Color online) Spatial radiation power of the electron under different laser intensities is projected onto the transverse plane perpendicular to the z-axis. Subplots (a)–(h) correspond to a_0 = 3, 4, 5, …, 10, respectively. The spatial radiation power is normalized to its own maximum value.

normalized to its own maximum value. The plane projection of the spatial radiation power has been added to the top of each figure for clearer observation and analysis. It is clear that the spatial distribution of the radiation power has an asymmetric bimodal structure. Moreover, increasing the laser intensity leads to a gradual decrease in the radiation angle range, indicating that the radiation emitted by the electron is better collimated.

In practical applications, researchers are more interested in the direction in which the maximum radiation power can be obtained. Therefore, we investigate the observation direction corresponding to the maximum radiation power $(dP/d\Omega)_{\max}$ and define the direction corresponding to $(dP/d\Omega)_{\max}$ as the direction of the maximum power radiation, denoted as $(\theta_{\max}, \varphi_{\max})$, namely,

$$\left[\frac{dP}{d\Omega}(\theta,\varphi)\right]_{\max} = \frac{dP}{d\Omega}(\theta_{\max},\varphi_{\max}). \tag{22}$$

In the polar coordinate system, the spatial distribution of the electron radiation is projected onto a two-dimensional plane to investigate the effects of the azimuth angle φ and the polar angle θ on the radiation power of the electron. [On the basis of numerical simulation, it was found that when θ is in the ranges of 0–15° and 60–180°, the radiation power of the electron is minor and negligible. Therefore, Fig. 6(b) only shows the radiation power of the electron in the range of θ = 15–60°.] It can be seen from Fig. 6 that the electron radiation power shows a clear nonuniform distribution on the azimuth angle φ and the polar angle θ, indicating that both have a significant effect on the observed maximum electron radiation power. Because of the periodicity of the azimuth angle φ, the spatial radiation power is actually continuous at 0° and 360°.

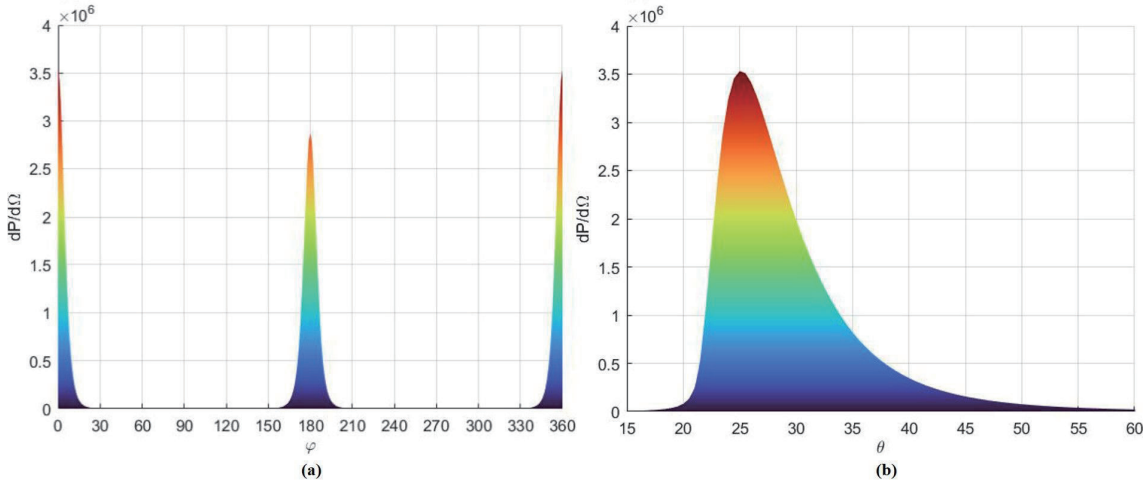

Fig. 6. (Color online) (a) Variation of the radiation power $dP/d\Omega$ with azimuthal angle φ when $a_0 = 6$. (b) Variation of $dP/d\Omega$ with polar angle θ when $a_0 = 6$. Both angles φ and θ are measured in degrees (°).

Table 1
Maximum power radiation directions (θ_{max}, φ_{max}) under different laser intensities.

Laser amplitude a_0	3	4	5	6	7	8	9	10
θ_{max} (°)	41	33	28	25	23	21.5	20.5	20
φ_{max} (°)	0	0	0	0	0	0	0	0

Specifically, the radiation power in Fig. 6(a) is concentrated in the ranges of φ = 0–30°, 150–210°, and 330–360°, and exhibits left–right symmetry with respect to the *xoz* plane. The extremum value of the radiation power is obtained at φ = 0° (or 360°) and φ = 180°, and reaches the global maximum at φ = 0° (or 360°). As shown in Fig. 6(b), the radiation power exhibits different distributions on either side of θ_{max}. When $\theta < \theta_{max}$, the radiation power increases rapidly within a narrow range, and when $\theta > \theta_{max}$, the radiation power decreases slowly. The maximum radiation power $(dP/d\Omega)_{max}$ is obtained at θ = 25°. Therefore, when the laser amplitude $a_0 = 6$, the maximum power radiation direction (θ_{max}, φ_{max}) = (25°, 0°).

The maximum power radiation directions under different laser intensities are studied, and the results are shown in Table 1. It can be found that as the laser intensity increases, φ_{max} remains unchanged at 0°, whereas θ_{max} gradually decreases from 41° to 20°, and the rate of decrease gradually slows down, indicating that a branch with the maximum radiation power $(dP/d\Omega)_{max}$ is gradually approaching the *z*-axis. It can be predicted that as the laser intensity increases, θ_{max} will infinitely approach 0°.

3.4 Time spectra characteristics

As shown in Fig. 7, the time spectra of the radiation power per unit solid angle $dP/d\Omega$ at the direction of the maximum power radiation (θ_{max}, φ_{max}) for different laser intensities were further investigated, and the microstructure of the peak amplitude in the time spectra was plotted. Table 2 shows the relevant simulated data for the time spectra.

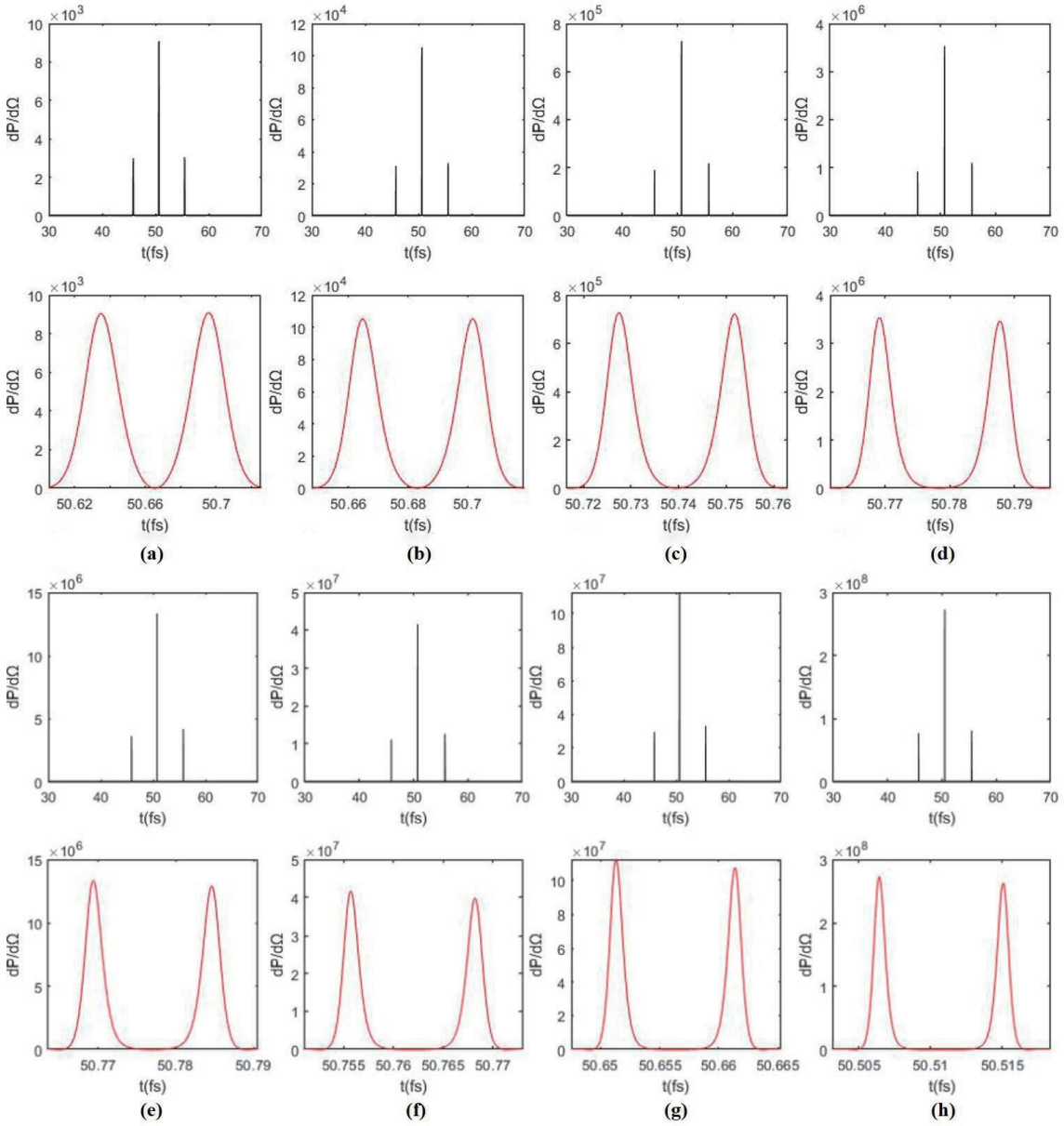

Fig. 7. (Color online) Temporal spectra (black lines) in the direction of maximum power radiation and the microstructure plots (red lines) of the amplitude peak are shown under different laser intensities. Subplots (a)–(h) correspond to a_0 = 3, 4, 5, …, 10, respectively.

Table 2
Maximum radiated power $(dP/d\Omega)_{max}$ and the corresponding time t_m under different laser intensities.

Laser amplitude a_0	3	4	5	6	7	8	9	10
t_m (fs)	50.7	50.7	50.7	50.8	50.8	50.7	50.7	50.6
$(dP/d\Omega)_{max}$	9.1×10^3	1.1×10^5	7.3×10^5	3.5×10^6	1.3×10^7	4.2×10^7	1.1×10^8	2.7×10^8

In Fig. 7 and Table 2, it can be observed that the time t_m at which the maximum radiation power $(dP/d\Omega)_{max}$ is obtained fluctuates around 50.7 fs, indicating that the time at which the

electron's maximum radiation power is obtained or measured under different laser intensities is basically stable. In addition, the time spectra show a clear three-peak structure, with the main peak significantly higher than the two subpeaks, indicating that the radiation power is mainly concentrated in a single pulse, i.e., the electron radiation power is mainly concentrated in the direction of the maximum power radiation. As depicted in Fig. 7, at the macroscopic level, it can be observed that the temporal spectra lose their symmetry when the laser is tightly focused, in contrast to the high symmetry revealed by the plane electromagnetic wave model used in Lee *et al.*'s work.[12] This is because the laser amplitude a_0 is the coefficient of the exponential term $\exp(-\eta^2/L^2-r^2/w^2)$ in the vector Eq. (7). As a_0 increases, the gradient of the vector equation becomes larger, leading to significant differences in acceleration at different positions and causing the temporal spectrum to lose its symmetry.

Furthermore, this asymmetry is also present at the microscopic level. In Fig. 7 (red line), it can be observed that each microstructure of the maximum-amplitude spike reveals a bimodal structure as a result of linear polarization, with each peak having its own different values. The maximum radiation power $(dP/d\Omega)_{max}$ obtained in Table 2 further confirms the conclusion we reached in Sect. 3.1: the maximum radiation power $(dP/d\Omega)_{max}$ varies exponentially with the laser amplitude a_0.

3.5 Frequency spectra characteristics

Finally, the spectral-angular distribution of the radiation energy per unit frequency interval per unit solid angle ($d^2I/d\omega d\Omega$) at different laser intensities was discussed, and the frequency spectral variation in the direction of the maximum power radiation (θ_{max}, φ_{max}) was studied, as shown in Fig. 8. To clearly present the data and to study the frequency spectra, the parts with relatively low intensity have been omitted, and each figure shows the best observed range of the frequency ω and polar angle θ. Table 3 shows the relevant simulated data for the frequency spectra in the direction of the maximum energy radiation at different laser intensities.

As shown in Fig. 8, the spectral angular distribution of the energy radiation (color maps) exhibits a similar pattern, with the radiation energy distributed as an 'arc-shaped mountain', with lower energy on the sides and higher energy in the center. As the laser intensity increases, the energy radiation expands toward higher frequencies (note that the frequency ω range varies in different subplots). When the laser intensity remains constant and the polar angle θ increases, the frequency bandwidth $\Delta\omega$ of the radiation gradually narrows. Combined with the data in Table 1, it was found that the region of concentrated radiation energy (red peaks of the mountain) and the maximum radiation energy $(d^2I/d\omega d\Omega)_{max}$ are located near the direction of the maximum power radiation ($\theta = \theta_{max}$). However, the polar angle θ corresponding to $(d^2I/d\omega d\Omega)_{max}$ is not equal to θ_{max}.

For the frequency spectra shown in Fig. 8 (black figure), the apparently disordered distribution can be attributed to the small-scale modulation in the motion of the electron owing to the limited pulse length, which leads to the harmonic offset and the formation of modulation spectra. The small-scale modulation is caused by the tiny differences in the time intervals between different radiation peaks [see Fig. 7 time spectra (black line)]. The large-scale

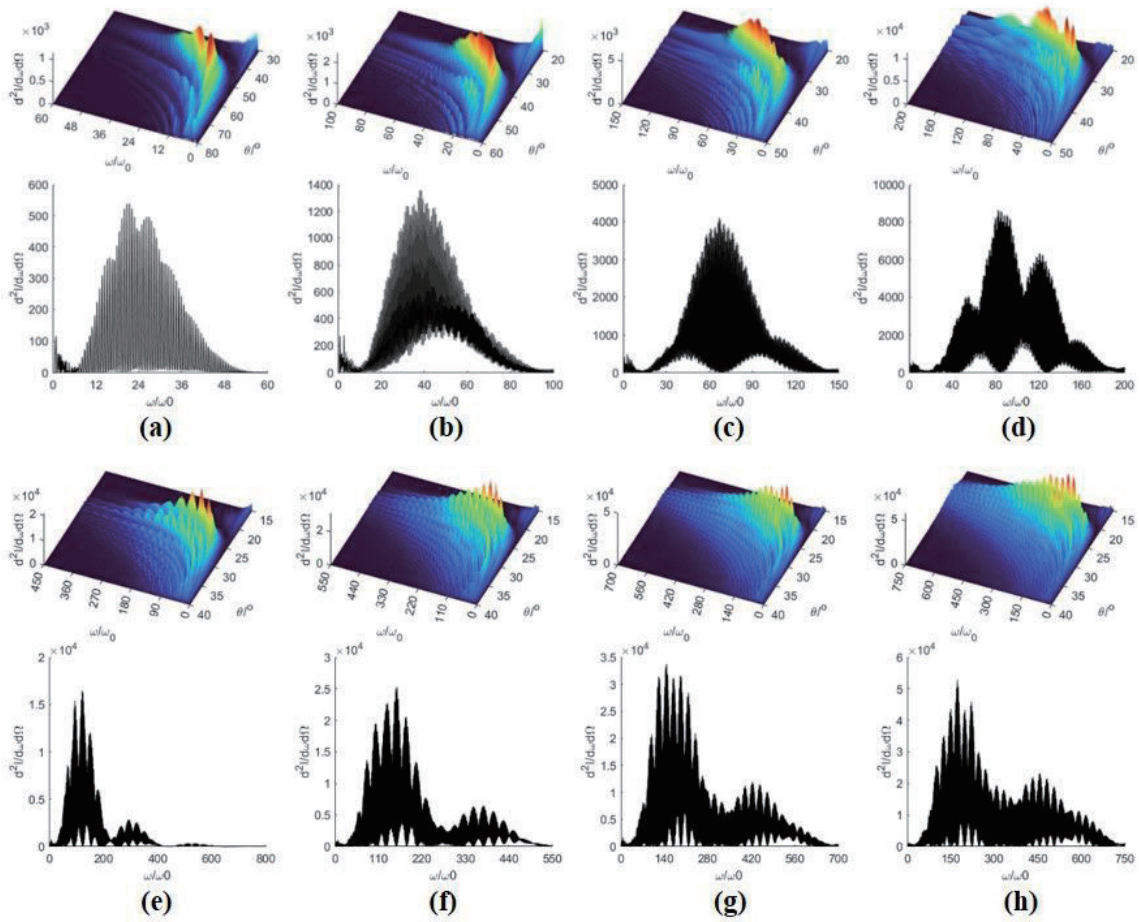

Fig. 8. (Color online) Spectral-angular distribution of the energy radiation (color maps) and the frequency spectra (black lines) of the maximum power radiation direction ($\theta = \theta_{max}$, given in Table 1) under different laser intensities. Subplots (a)–(h) correspond to a_0 = 3, 4, 5, …, 10, respectively. Note that in order to present the data clearly, the radiation intensity is normalized to its maximum value, and the ranges of ω and θ vary in each figure.

Table 3
Maximum radiation energy $(d^2I/d\omega d\Omega)_{max}$ and the corresponding frequency ω_{max} under different laser intensities.

Laser amplitude a_0	3	4	5	6	7	8	9	10
ω_{max}/ω_0	21.4	38.0	66.8	82.5	120.9	136.3	147.0	172.8
$(d^2I/d\omega d\Omega)_{max}$	5.4×10^2	1.4×10^3	4.1×10^3	8.7×10^3	1.6×10^4	2.5×10^4	3.3×10^4	5.3×10^4

modulation is caused by the bimodal structure of radiation [see Fig. 7 microstructure plots (red line)], which describes the overall variation trend of the envelope. When the laser amplitude a_0 = 3, the range of large-scale modulation (the frequency range contained in the first envelope on the left side of the frequency spectrum) is about $60\omega_0$. As the laser intensity $I_0\left(a_0 \in [3,10]\right)$ increases, the interval of large-scale modulation gradually increases and finally reaches about $380\omega_0$ when a_0 = 10. According to Table 3, the maximum radiation energy $(d^2I/d\omega d\Omega)_{max}$ and its

corresponding frequency ω_{max} exhibit an increasing trend. $(d^2I/d\omega d\Omega)_{max}$ increases from 540 to 5.3×10^4, whereas ω_{max} shifts from the right of $21.4\omega_0$ to $172.8\omega_0$.

4. Conclusions

As a novel type of X-ray source, RNTS can be widely used in the field of optical imaging. In this work, the effects of linearly polarized tightly focused Gaussian laser pulses with different laser intensities on the optimal position and spatial radiation characteristics of the electron in the RNTS process are studied. We report the first discovery of a significant linear relationship between the optimal position of the electron z_0 and the laser amplitude a_0, with the mathematical expression as $z_0 = -2 \times a_0 + 3$. In addition, the maximum radiation power $(dP / d\Omega)_{max}$ changes exponentially with a_0, with a fitting result of $(dP / d\Omega)_{max} = 25850 \times e^{0.93a_0}$. After interacting with the laser pulse, the electron always oscillates first along the +z-axis and then moves linearly within the xoz plane, with an asymmetric trajectory. As the laser intensity increases, the radiation space gradually becomes smaller and the collimation becomes better. In the direction of maximum power radiation, the azimuth angle φ stays at 0°, whereas the corresponding polar angle θ is reduced from 41° to 20°, and the spatial radiation is close to the z-axis.

Moreover, the time spectra and frequency spectra in the direction of the maximum power radiation are further investigated. As the laser intensity increases, it reveals that the peak arrival time with the maximum amplitude is basically stable around 50.7 fs. As the laser intensity increases, the frequency spectra exhibit an expansion of the large-scale modulation interval, which ranges from about $60\omega_0$ for $a_0 = 3$ to about $380\omega_0$ for $a_0 = 10$. Please note that our research and analysis are based primarily on theoretical modeling and numerical simulation. In practical experimental processes, it is necessary to deal with external environmental factors such as temperature jumps or thermal shock.[21,22] If possible, these factors will be further investigated by controlling the motion of electrons and the parameters of laser pulses in future work.

The results of this study provide valuable insights for researchers to more efficiently determine the optimal position and observation direction of the electron according to the current laser intensity, in order to make more efficient use of RNTS, and thus provide high-power and ultrashort X-rays for optical imaging.

Acknowledgments

This work has been supported by the National Natural Sciences Foundation of China under Grant Nos. 10947170/A05 and 11104291, natural science fund for colleges and universities in Jiangsu Province under Grant No. 10KJB140006, Natural Sciences Foundation of Shanghai under Grant No. 11ZR1441300, and Natural Science Foundation of Nanjing University of Posts and Telecommunications under Grant No. NY221098 and sponsored by the Jiangsu Qing Lan Project and STITP Project under Grant No. XYB2022012.

References

1 C.-C. Lee, S.-T. Tsai, and C.-H. Yang: Sens. Mater. **30** (2018) 1859. https://doi.org/10.18494/sam.2018.1899
2 H. Kato, T. Fujiwara, B. E. O'Rourke, H. Toyokawa, A. Koike, T. Aoki, and R. Suzuki: Sens. Mater. **28** (2016) 763. https://doi.org/10.18494/sam.2016.1249
3 P. Suortti and W. Thomlinson: Phys. Med. Biol. **48** (2003) R1. https://doi.org/10.1088/0031-9155/48/13/201
4 Z. Chi, Y. Du, W. Huang, and C. Tang: J. Synchrotron Radiat. **27** (2020) 737. https://doi.org/10.1107/s1600577520003574
5 P. Maine, D. Strickland, P. Bado, M. Pessot, and G. Mourou: IEEE J. Quantum Electron. **24** (1988) 398. https://doi.org/10.1109/3.137
6 M. D. Perry and G. Mourou: Science **264** (1994) 917. https://doi.org/10.1126/science.264.5161.917
7 T. Eidam, S. Hanf, E. Seise, T. V. Andersen, T. Gabler, C. Wirth, T. Schreiber, J. Limpert, and A. Tünnermann: Opt. Lett. **35** (2010) 94. https://doi.org/10.1364/ol.35.000094
8 A. Dubietis, G. Jonušauskas, and A. Piskarskas: Opt. Commun. **88** (1992) 437. https://doi.org/10.1016/0030-4018(92)90070-8
9 W.-Q. Ji, Q. Wei, X.-F. Zhu, D.-J. Wu, and X.-J. Liu: Europhys. Lett. **125** (2019) 58002. https://doi.org/10.1209/0295-5075/125/58002
10 I. V. Pogorelsky, I. Ben-Zvi, T. Hirose, S. Kashiwagi, V. Yakimenko, K. Kusche, P. Siddons, J. Skaritka, T. Kumita, A. Tsunemi, T. Omori, J. Urakawa, M. Washio, K. Yokoya, T. Okugi, Y. Liu, P. He, and D. Cline: Phys. Rev. Accel. Beams **3** (2000) 090720. https://doi.org/10.1103/physrevstab.3.090702
11 W. Yan, C. Fruhling, G. Golovin, D. Haden, J. Luo, P. Zhang, B. Zhao, J. Zhang, C. Liu, M. Chen, S. Chen, S. Banerjee, and D. Umstadter: Nat. Photonics **11** (2017) 514. https://doi.org/10.1038/nphoton.2017.100
12 K. Lee, Y. H. Cha, M. S. Shin, B. H. Kim, and D. Kim: Phys. Rev. E **67** (2003) 026502. https://doi.org/10.1103/physreve.67.026502
13 K. Li, L. Li, Q. Shu, Y. Tian, Y. Shi, and Z. Zhang: Optik **183** (2019) 813. https://doi.org/10.1016/j.ijleo.2019.02.154
14 Y. Wang, C. Wang, K. Li, L. Li, and Y. Tian: Opt. Quantum Electron. **53** (2021) 229. https://doi.org/10.1007/s11082-021-02870-7
15 X.-R. Hong, Y.-N. Li, D. Wei, R.-A. Tang, J.-A. Sun, and W.-S. Duan: Phys. Plasmas **29** (2022) 043102. https://doi.org/10.1063/5.0077486
16 J. Zhuang, Y. Wang, C. Wang, Y. Cai, and Y. Tian: Laser Phys. **31** (2021) 065403. https://doi.org/10.1088/1555-6611/abfa89
17 Y. Yan, X. Zhou, and Y. Tian: Opt. Quantum Electron. **54** (2022) 865. https://doi.org/10.1007/s11082-022-04162-0
18 A. V. Borovskiy and A. L. Galkin: Laser Phys. Lett. **18** (2021) 066002. https://doi.org/10.1088/1612-202x/abf8a4
19 H. Lee, S. Chung, K. Lee, and D. Kim: New J. Phys. **10** (2008) 093024. https://doi.org/10.1088/1367-2630/10/9/093024
20 D. Kim, H. Lee, S. Chung, and K. Lee: New J. Phys. **11** (2009) 063050. https://doi.org/10.1088/1367-2630/11/6/063050
21 J.-H. He and N. Y. Abd Elazem: Energies **14** (2021) 6691. https://doi.org/10.3390/en14206691
22 F. Liu, T. Zhang, C.-H. He, and D. Tian: Facta Univ. Ser.: Mech. Eng. **20** (2022) 633. https://doi.org/10.22190/fume210317054l

About the Authors

Han-Chen Qiu is currently studying for a bachelor's degree at Nanjing University of Posts and Telecommunications, China. His research interests include deep learning and nonlinear optics. (b20031912@njupt.edu.cn)

You-Wei Tian has been an associate professor at Nanjing University of Posts and Telecommunications since 2007. He received his Ph.D. degree from the Chinese Academy of Sciences in 2007 and has published a total of 48 academic papers, 30 of which have been included in SCI. His research interests include laser field and electronic information detection, laser–matter interaction, and other related fields. (tianyw@njupt.edu.cn)

Chih-Cheng Chen has been a professor at Jimei University, China, since 2017. He became a member of IEEE in 2011 and a senior member in 2016. He earned his M.S. degree in 2005 and recently earned his Ph.D. degree from the Department of Mechatronics Engineering, National Changhua University of Education. He has published 43 academic articles and owns three patents. He has also spearheaded several projects funded by the National Natural Science Foundation of China, Fujian Province. His research interests include AIoT technology, machine learning, information security, and RFID applications. (chenccheng@fcu.edu.tw).